Journal of Microscopy

Journal of Microscopy, Vol. 251, Issue 1 2013, pp. 99–107 doi: 10.1111/jmi.12050
Received 11 January 2013; accepted 18 April 2013

Phase-retrieved pupil function and coherent transfer function in confocal microscopy

M.R. FOREMAN*,†, C.L. GIUSCA*, P. TÖRÖK* & R.K. LEACH†
*Blackett Laboratory, Department of Physics, Imperial College London, Prince Consort Road, South Kensington, London, UK
†Engineering Measurement Division, National Physical Laboratory, Hampton Road, Teddington, Middlesex, UK

Key words. Confocal microscopy, 3D transfer function, phase retrieval.

Summary

This work reports on the retrieval of the pupil function and coherent transfer function of a coherent reflection type confocal microscope from simulated measurements of the intensity point spread function. Two phase retrieval algorithms are presented in this vein, which incorporate the multiple pupil dependence of image formation in confocal microscopy. Verification of the algorithms follows by numerical simulations.

Introduction

With the growing popularity of optical measurements in high-precision nanometrology the need for full system characterization has become of paramount importance (Leach *et al.*, 2012). For example, an important issue that must be addressed to bring surface topography measurements into compliance with manufacturing quality systems is the measurement traceability of the instruments. Calibration protocols and evaluation techniques using bespoke primary instrumentation currently exist, such as those detailed in Giusca *et al.* (2011, 2012); however, these consider only a limited number of system parameters, such as instrument flatness, amplification coefficients and linearity and squareness of the scales, and thus do not provide a complete system description. Current trends in microscopy and three-dimensional (3D) imaging towards quantitative measurements furthermore require a complete understanding of the relevant optical imaging characteristics. Localization accuracy in localization microscopy is, for example, highly dependent on the assumed point spread function (PSF) used for data fitting. Since the PSF is realistically strongly dependent on system aberrations, such information is key for accurate data analysis and system benchmarking (Cotte *et al.*, 2010; Stallinga & Rieger, 2010; Cole *et al.*, 2011; Mandal *et al.*, 2012; Quirin *et al.*, 2012).

It has long been recognized that complete specification of linear optical systems can be obtained by determining either the 3D PSF or the associated transfer function. Indeed, among the many alternative imaging configurations which currently exist, such as fluorescence, interferometric and so-called conventional modalities, previous work has detailed numerous theoretical and empirical results regarding the PSF and its associated Fourier representation (see Gu, 1996; Foreman *et al.*, 2013, for a fuller review). Incoherent imaging systems, such as fluorescence-based systems, act as linear filters of the scattered optical intensity of an object such that they can be characterized using an intensity point spread function (IPSF). Coherent imaging systems, however, act as a linear filter on the scattered *field amplitude* and the amplitude point spread function (APSF) must instead be used so as to conserve phase information. Equivalently, the Fourier representations of the IPSF and APSF, known as the optical transfer function (OTF) and coherent transfer function (CTF), respectively, can also be used.

Experimental determinations of the IPSF or OTF for incoherent imaging systems are commonplace in the literature (see Foreman *et al.*, 2013); however, due to the necessity to measure complex field amplitudes in coherent systems, measurements of the APSF and CTF are less prevalent. Of those accounts reported, such measurements are predominantly approached by means of interferometry. For example, Selligson (1981) and Dändliker *et al.* (2004) have used a Mach–Zender interferometer to measure the aberrations present in a lens by mapping the phase and IPSFs in the lens' focal region. Similarly, Schrader & Hell (1996), Zhou & Sheppard (1997) and Török & Kao (2002) have reported use of Tywman–Green interferometers for measurements of APSFs, whereas Juškaitis & Wilson (1997) and Walford *et al.* (2002) have further employed fibre optic interferometers. Digital holographic measurements have also recently been reported (Marian *et al.*, 2006; Cotte *et al.*, 2010).

Correspondence to: Matthew R. Foreman, Blackett Laboratory, Department of Physics, Imperial College London, Prince Consort Road, South Kensington, London, SW7 2BZ, UK. Tel: +44 (0)20 7594 7721; fax: +44 (0)20 7594 7714; e-mail: matthew.foreman@imperial.ac.uk

Despite the extensive use of interferometric methods, non-interferometric methods may be preferable in some circumstances. Wavefront sensing systems, for example, are commonly used in scenarios where phase perturbations are strong, rapidly changing and broadband, such as imaging through the atmosphere. In this vein, Beverage *et al.* (2002) have used a Shack–Hartmann sensor placed at the exit pupil of a microscope to measure the exit wavefront from which the PSF can be found via a Fourier transform (*cf.* Eq. 5). In other scenarios, such as the calibration of preexisting industrial set-ups, avoiding the need of additional optics and system modification is preferable. Here, use of phase retrieval algorithms (Gureyev *et al.*, 1995; Almoro *et al.*, 2006; Maiden & Rodenburg, 2009; Sakamoto & Barrett, 2012), which use wave propagation laws to extract phase information from intensity only images, present a further noninterferometric technique. In the context of optical imaging, phase retrieval algorithms have successfully been applied in wide-field and fluorescence microscopy for retrieval of the complex pupil function and APSF (Hanser *et al.*, 2004). Despite the pervasiveness of coherent confocal imaging systems; however, the use of phase retrieval algorithms in a coherent confocal imaging set-up can currently not be found in the literature, much to the authors' surprise. The apparent difficulty arises since, in conventional phase recovery algorithms, a single pupil is assumed. In confocal microscopy, however, both the pupil function of the objective and collecting lens play a role in the image formation, such that the single pupil requirement is not satisfied.

Fortunately, traditional phase retrieval algorithms can be easily modified to allow their successful use in a confocal set-up to retrieve either the two-dimensional (2D) pupil function or the 3D CTF. This paper reports on these modifications and provides proof-of-principle results by way of verification. Hence, the imaging model for a high numerical aperture (NA) reflection mode confocal microscope is first briefly presented in the Section 'Confocal imaging model', before the modified phase retrieval techniques for extraction of the complex 2D pupil function (Section 'Algorithm 1: retrieval of the 2D pupil function') and the 3D CTF (Section 'Algorithm 2: retrieval of the 3D CTF') are discussed. Numerical verification of these algorithms, using a set of simulated aberrated confocal images, is presented in Section 'Simulation results'.

Confocal imaging model

In a confocal microscope, both illumination and detection optics contribute equally to image formation. Specifically, a point source (assumed to be on-axis) is imaged onto the object of interest by means of an objective lens L_1 and the light scattered by the sample is imaged onto a point detector (also assumed to be on-axis) by means of a collector lens L_2. The 3D APSF of the imaging system, $h(\mathbf{r})$, can be shown to be given by the product of the APSF of both lenses, *viz.*

$$h(\mathbf{r}) = h_1(\mathbf{r})h_2(\mathbf{r}), \tag{1}$$

where $\mathbf{r}$ is a position vector in object space. Given that only a small area of the object is illuminated, a complete image is built up by scanning either the illumination beam (and synchronously the detection beam) across the object, or by physically scanning the object position. The latter can help to maintain shift invariance of the imaging system (Gu, 1996) and will hence be assumed here. Therefore, and further adopting a scalar approximation, the image field from an arbitrary object can be written as

$$U(\mathbf{r}_s) = \iiint h(\mathbf{r})t(\mathbf{r}-\mathbf{r}_s)d\mathbf{r} = \iiint h(\mathbf{r}-\mathbf{r}_s)t(\mathbf{r})d\mathbf{r}, \tag{2}$$

where $\mathbf{r}_s$ denotes the scan position of the object, $t(\mathbf{r})$ is the scattering potential of the object and the integration is performed over the full extent of the object.

Equivalently, a frequency domain description can be adopted whereby

$$U(\mathbf{r}_s) = \iiint \widetilde{h}(\mathbf{m})\widetilde{t}(\mathbf{m}) \exp[2\pi i \mathbf{r}_s \cdot \mathbf{m}]\, d\mathbf{m}, \tag{3}$$

where $\widetilde{h}(\mathbf{m})$ is the 3D CTF of the system, and $\widetilde{t}(\mathbf{m})$ is the scattering spectrum; $\mathbf{m} = (m, n, s)$ is a triplet of spatial frequencies in the (x, y, z) directions, such that integration is performed over the whole spatial frequency domain. The APSF and the CTF are related by a 3D Fourier transform, *viz.*

$$\widetilde{h}(\mathbf{m}) = \iiint h(\mathbf{r}) \exp[-2\pi i \mathbf{r} \cdot \mathbf{m}]\, d\mathbf{r} \tag{4}$$

and the associated inverse relation (and similarly for $\widetilde{t}(\mathbf{m})$ and $t(\mathbf{r})$). It can however be further noted that the APSF of each individual lens is given by

$$h_j(\mathbf{m}) = \iiint P_j(m, n)S(\mathbf{m}) \exp[2\pi i \mathbf{r} \cdot \mathbf{m}]\, d\mathbf{m} \tag{5}$$

for $j = 1$ or 2. $P_j(m, n)$ is known as the pupil function and describes apodization and phase perturbations in the pupil of L_j. The factor

$$S(\mathbf{m}) = \frac{1}{s}\, \delta[s - (1/\lambda^2 - m^2 - n^2)^{\frac{1}{2}}] \tag{6}$$

is required for a more accurate description of high NA lenses (see, e.g. Gu, 1996; Hanser *et al.*, 2003).

Via Eqs. (1), (4) and (5), the 3D CTF can then be written as the 3D convolution of the pupil function of each lens, i.e.

$$\widetilde{h}(\mathbf{m}) = [P_1(m, n)S(m, n)] \otimes_3 [P_2(m, n)S(m, n)]\,. \tag{7}$$

Equation (7) illustrates the additional complication of image formation in confocal microscopy, namely that it is dependent on two pupils. Existing phase retrieval algorithms, such as those presented in Hanser *et al.*, 2004, 2003; Almoro *et al.*, 2006, assume a single pupil and hence fail when applied to confocal images. However, for a reflection mode

confocal system a single lens is commonly used to perform the role of both the objective and collector lens. Accordingly, $h_1(\mathbf{r}) = h_2(\mathbf{r}) = h_{1,2}(\mathbf{r})$, such that

$$h(\mathbf{r}) = h_{1,2}^2(\mathbf{r}) \tag{8}$$

and the pupil functions are identical, i.e. $P_1(m, n) = P_2(m, n) = P_{1,2}(m, n)$. Consequently, a simple modification of existing algorithms can be made to allow full phase information to be iteratively retrieved in a confocal imaging system, as shall be discussed in the next section. As a final point, it should be noted that Eq. (8) is also applicable to a reflection geometry in which two lenses are used with equal amounts of defocus. Similarly, for a transmission set-up, Eq. (8) holds if the illumination and detection lenses have equal but opposite defocus. Accordingly, the algorithms presented below are also applicable in these cases.

Phase retrieval algorithm

In this paper, two alternative algorithms are presented capable of determining the full 3D imaging properties of a coherent reflection type confocal microscope from an intensity only image of a point-like object. Specifically, the first retrieves the complex valued pupil function $P_{1,2}(m, n)$ from the IPSF. The CTF can then be determined via Eq. (7) if desired. The second algorithm extracts the CTF directly from a measurement of the IPSF. It is noted that this is not merely a 3D Fourier transform as would be the case for an incoherent system.

Algorithm 1: retrieval of the 2D pupil function

Phase retrieval by means of variants and generalizations of the Gerchberg–Saxton algorithm is well documented. In general, such algorithms require an intensity distribution to be known on at least two distinct planes within the optical system. For example, a pure Gerchberg–Saxton algorithm assumes the source and target intensity distributions are known (Gerchberg & Saxton, 1972), whereas by means of propagation equations, knowledge of two planes within a 3D target distribution can be used (Hanser *et al.*, 2004; van der Avoort *et al.*, 2005; Pedrini *et al.*, 2005; Almoro *et al.*, 2006; Migukin *et al.*, 2011). If a 3D data set, e.g. from multiple plane observations, is acquired, data are invariably averaged along the axial direction to improve robustness of existing phase retrieval algorithms. In a focusing and imaging context, these techniques have hence proven successful in determining the 2D imaging properties of a lens or imaging system (Hanser *et al.*, 2004; van der Avoort *et al.*, 2005). For a coherent confocal reflection set-up, these properties are contained in the pupil function $P_{1,2}(m, n)$. Therefore, a modification of the algorithm of Hanser *et al.* (2004), which originally aimed to retrieve the pupil function in wide-field fluorescence imaging from IPSF measurements, is presented here. The outline of this modified algorithm (which shall be referred to as Algorithm 1) is depicted in Figure 1 and operates as follows:

- First, an initial guess of the pupil function $P_{1,2}(m, n)$ is made, which for the purposes of the calculations presented in this paper was taken as a uniform amplitude transmittance with uniform phase, limited by the finite aperture of the lens.
- Given this pupil function, a defocus is analytically applied for each PSF section, by means of multiplication by a propagation factor $\exp[i2\pi\Delta z s]$, where Δz is the axial distance of each PSF section from the focal plane.
- Each defocused pupil function is then used to determine an estimate of the PSF of a single lens at the associated defocused planes by means of Eq. (5).
- The amplitude of the resulting single lens PSF is replaced by the *fourth* root of the measured confocal intensity images and a new defocused pupil determined for each PSF section by means of the inverse of Eq. (5).
- An average pupil function is then calculated from all defocused pupils to form a new input pupil function for which the above algorithm is repeated. Constraints, such as a finite NA restriction, and smoothing operations may also be applied at this point. Iteration proceeds until a convergence criterion or other exit condition is met.

When the above algorithm is compared with that of Hanser *et al.* (2004), it is seen that the main difference lies in the fact that the fourth root of the intensity images is used to update the iterative calculations as opposed to the square root. The origin of this difference is perhaps easiest to see from inspection of Eq. (1), whereby it is evident that the total PSF is formed of the product of two individual (identical) PSFs, producing an additional exponent which needs to be accounted for. Given the pupil function, $P_{1,2}(m, n)$, Eq. (7) can be used to determine the 3D CTF describing the 3D imaging properties of the imaging system.

Similar modification of the algorithm presented in Almoro *et al.* (2006) has also been made such that the phase information of confocal image stacks of point objects can also be retrieved without the need to directly calculate the pupil function. These results are not presented here.

Algorithm 2: retrieval of the 3D CTF

Three-dimensional information contained within an IPSF, instead of being averaged along the axial direction, can alternatively be used to determine the full 3D CTF of a system. Figure 2 depicts the principles behind an algorithm (which shall be referred to as Algorithm 2) suitable for direct computation of the 3D CTF of a coherent confocal reflection imaging system, from an IPSF. The parallels with the Gerchberg–Saxton algorithm should be evident, however, the detailed steps are as follows:

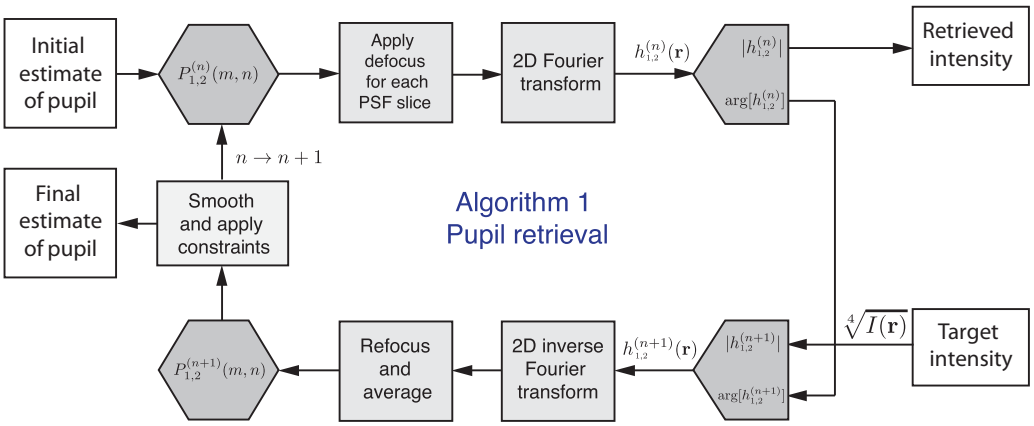

Fig. 1. Schematic of the algorithm used to extract the pupil function of a reflection mode confocal microscope.

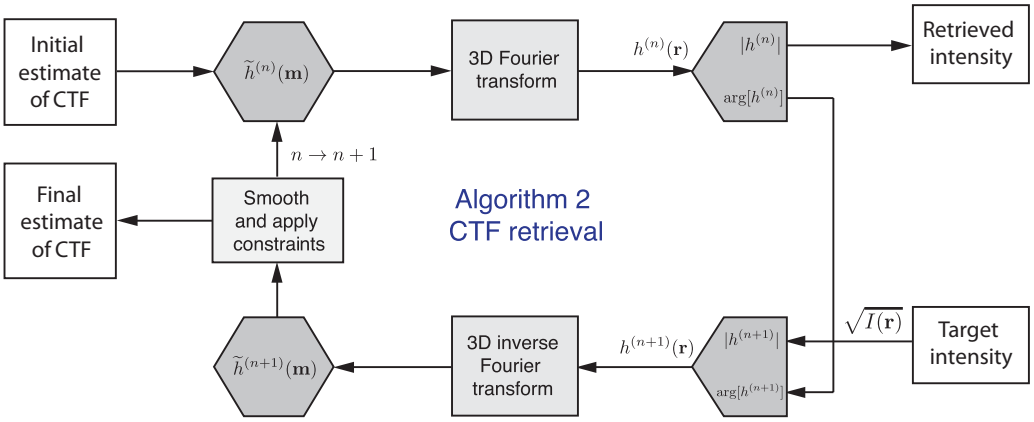

Fig. 2. Schematic of the algorithm used to extract the CTF of a reflection mode confocal microscope.

- First, an initial guess of the CTF is made, which for the purposes of the calculations is taken as the analytic expressions given in Gu (1996) for an ideal reflection mode confocal microscope.
- Given this CTF, an estimate of the image field is calculated by means of Eq. (3). The amplitude of the resulting image field is replaced by the square root of the measured intensity images.
- A new CTF is then calculated by using the inverse of Eq. (3), i.e. inverse Fourier transform. The algorithm is repeated with the new estimate of the CTF as initial input. Constraints, such as a finite NA restriction, and smoothing operations may also be applied at this point. Iteration again proceeds until a convergence criterion or other exit condition is met.

It should be noted that this algorithm makes no reference to the existence of a pupil function. Accordingly, this algorithm is suitable for determination of imaging properties for systems which do not possess an axial-independent pupil function, such as recently proposed rotating beams (Quirin *et al.*, 2012).

Simulation results

To serve as test input for both of the algorithms presented above, imaging of a point object by a reflection mode confocal microscope was simulated and a 3D stack of synthetic images generated. Phase aberrations were assumed to be present in the system, as described by the pupil function $P(m, n) = \exp[i\,W(m, n)]$, where $W(m, n)$ is a phase term represented by a sum of Zernike aberrations (Born & Wolf, 1980), i.e.

$$W(m,n) = \sum_{p=0}^{\infty} \sum_{\substack{q=-p \\ p-q \text{ even}}}^{p} a_{pq}\, R_p^q(\lambda\sqrt{m^2+n^2}) \exp[iq\varphi],$$

where a_{pq} are the Zernike coefficients describing the strength of each aberration, $R_p^q(\rho)$ are the Zernike polynomials and

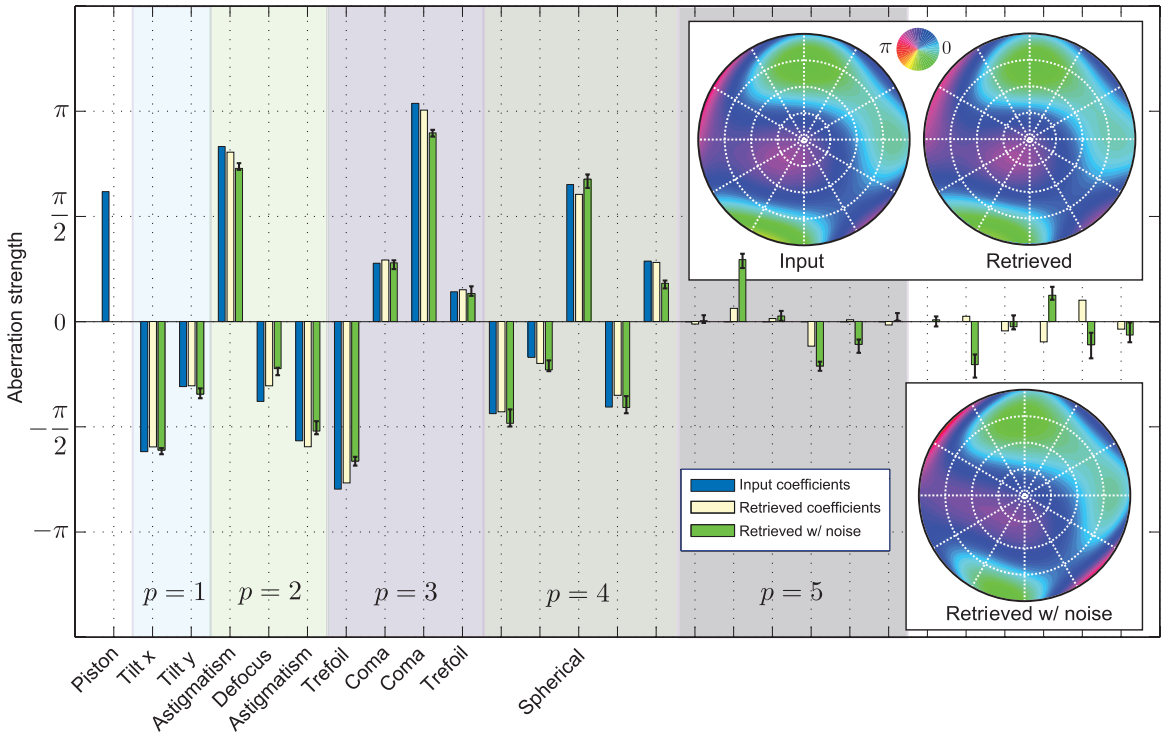

Fig. 3. Bar chart showing a comparison between the ground truth aberration coefficients and those retrieved using Algorithm 1 for noise-free and noisy data. Error bars depict the maximum and minimum of the retrieved coefficients from all realizations. Insets show the retrieved phase of the pupil functions in each case.

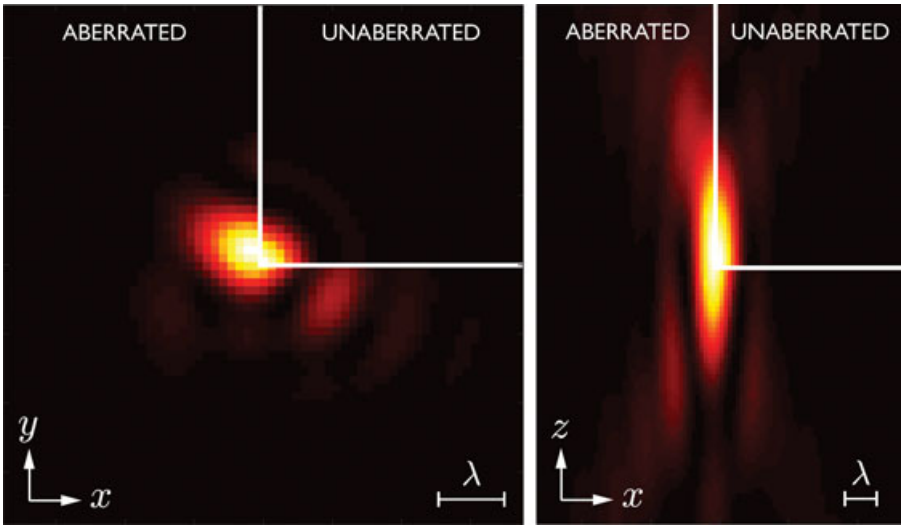

Fig. 4. Transverse (left) and axial (right) cross-sections of aberrated $\sqrt{\text{IPSF}}$, used during phase retrieval simulations. Insets show unaberrated case for reference. Field of view has been truncated for display purposes only.

$\varphi = \arctan(n/m)$. Specifically, aberrations up to order $p = 4$ were assumed to have nonzero Zernike coefficient. The weighting associated with each aberration type is shown in Figure 3 whereby it is seen that strong astigmatism, trefoil, coma and spherical aberration were included. The 3D IPSF data were calculated over a field of view of dimensions 10 μm × 10 μm × 10 μm, sampled at 80 nm in the x and y-directions and at 100 nm in the axial direction. Transverse and axial cross-sections of the magnitude of the APSF (i.e. $\sqrt{\text{IPSF}}$) are shown in Figure 4. Note that the magnitude of the

APSF is plotted as opposed to the IPSF for increased contrast only, and that the unaberrated case is also shown for reference purposes. An NA of 0.6 and a wavelength of $\lambda = 670$ nm was assumed throughout simulations. Fourier transforms were implemented using a chirp-z transform, so as to avoid the need for zero padding and other sampling issues.

Algorithm 1 was first tested by using the synthetic 3D IPSF images as input data. The argument of the complex pupil function retrieved by Algorithm 1 after 50 iterations, was subsequently decomposed into its constituent Zernike aberrations up to order $p = 6$ using the method of moments, and the resulting aberration coefficients compared to those input. Retrieved aberration coefficients, assuming noise-free images are shown in Figure 3, whereby it is seen that there is good agreement between the input and retrieved coefficients. Nonzero coefficients for Zernike aberrations of order $p > 4$ are, however, obtained and arise due to numerical noise introduced by finite sampling and pixellation of the ideal images. Other discrepancies arise for the same reason and reduce with increased sampling rates.

Further simulations were also performed, whereby additive Gaussian noise, with a signal-to-noise (SNR) ratio of 10^3, was used to corrupt the synthetic images. Before applying Algorithm 1, noisy data were preprocessed. Specifically, the mean background was subtracted (as was determined by averaging a small portion of the images far from the optical axis) and a bandpass filter (as determined by the NA) was applied. A total of 200 noise realizations were simulated and the aberration coefficients calculated in each case. The mean of all realizations is also plotted in Figure 3. The accompanying error bars depict the maximum and minimum of the retrieved coefficients from all realizations. It should be noted that due to the nonlinear dependence of the retrieved phase on the input intensity, a bias can be introduced into the retrieved coefficients in the presence of noise (Sakamoto & Barrett, 2012), which can also be seen in Figure 3. Similar Monte Carlo simulations were also performed for SNRs ranging from 10^{-1} to 10^5. For each case, the mean of the integrated root mean square (RMS) phase error between the retrieved and true phase profiles averaged over the pupil was determined and is shown in Figure 5. A clear downward trend is evident for increasing SNR as would be expected, however it is noted that for SNRs $< 10^{-1}$ Algorithm 1 performs poorly. More sophisticated preprocessing algorithms are, however, expected to improve final phase retrieval results.

For further comparison, the upper insets of Figure 3, show the argument of the input pupil function (i.e. the phase distortions introduced by the lens) and that retrieved in the noise-free case. A global phase difference has been removed for ease of comparison. The amplitude of the retrieved pupil (not shown) exhibits a highly uniform distribution in excellent agreement to the ground truth. The lower inset shows the phase of a typical retrieved pupil function from noise corrupted images (SNR $= 10^3$). The absolute mean integrated phase error across the pupil for the noise-free and noisy case is equivalent to 0.011 and 0.025 waves, respectively. In all simulations, a finite NA constraint was implemented and the argument of the pupil function constrained to be a superposition of Zernike aberrations up to order $p = 6$. A Gaussian smoothing filter was also applied to the amplitude of the pupil every five iterations.

Although good performance has been demonstrated in the numerical simulations above, it should be noted that due to the additional exponent involved in the update function for Algorithm 1, the algorithm is less robust to noise as compared to the equivalent wide-field algorithm presented in Hanser *et al.* (2004). By taking the fourth root of the confocal image stack, any noise present is amplified, thus reducing the effective SNR in a nonlinear fashion. Indeed, comparable performance between Algorithm 1 and its wide-field equivalent, in terms of the errors on the retrieved aberration coefficients, is found when $\mathrm{SNR}_{\mathrm{confocal}} \approx \mathrm{SNR}^2_{\mathrm{wide\text{-}field}}$ As shown in Figure 2, however, Algorithm 2 uses the square root of the confocal intensity images as the update function and consequently noise is amplified to a lesser extent (and to a comparable level to that of the wide-field pupil retrieval algorithm presented in Hanser *et al.*, 2004). That said, however, Algorithm 2 lacks any improvement in effective SNR gained by averaging data from multiple axial planes. It is hence not immediately obvious which algorithm would be expected to have superior performance. To compare the convergence of Algorithms 1 and 2, the total relative RMS error between the true (normalized) IPSFs and those iteratively retrieved is compared for a noise-free case (and without smoothing) in Figure 5 as a function of the number of algorithm iterations. To investigate the balance of these two effects, a number of sampling scenarios were considered. Good convergence behaviour is seen in all cases, with RMS error plateauing after as few as ~ 20 iterations at values of $\sim 10^{-3}$, albeit a small downward trend is still exhibited in the data for Algorithm 2. In general, comparable performance is seen between both algorithms, however, it is evident that increased sampling in the axial direction, in turn implying more confocal planes are input into the algorithms, reduces the total RMS error. For example, Figure 5 shows that halving the axial sample spacing, δz, from 100 to 50 nm, gives rise to a reduction of $\sim 25\%$ in final RMS error. Interestingly, if the axial extent of the confocal stack is increased from $\Delta z = 10$ to $\Delta z = 20$ μm the performance of Algorithm 1 worsens, whereas that of Algorithm 2 is relatively unchanged. This behaviour can be understood because by increasing the axial range of the confocal image stack, confocal planes with very weak signal are included in the data input into the retrieval algorithms. For Algorithm 1, these planes merely add noise to the averaged quantities, whereas for Algorithm 2, planes with weak signal still contain important information regarding the 3D imaging properties of the system and thus do not greatly affect the RMS error, although a slight performance degradation can be seen. With regards to convergence properties when noisy images are used as input data, it is important

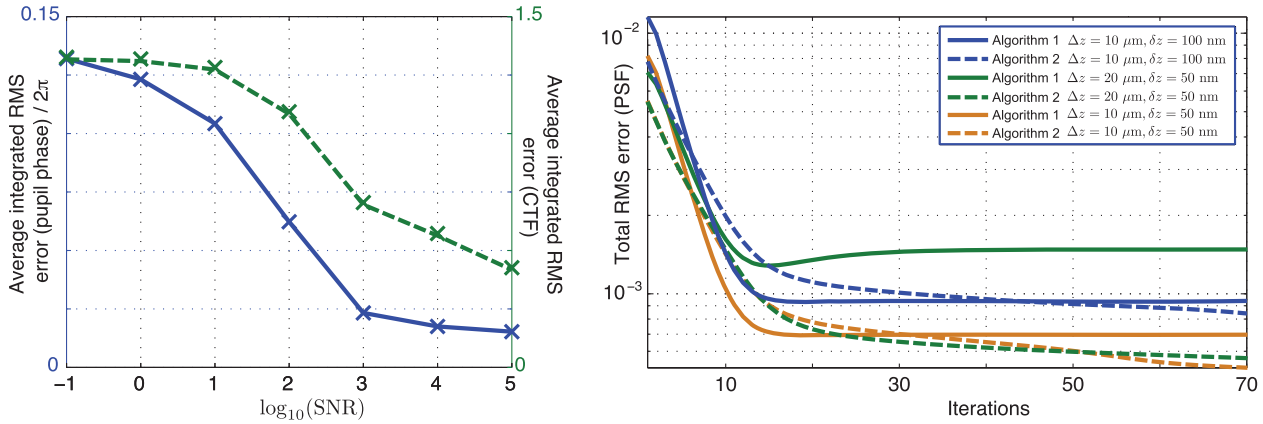

Fig. 5. (Left) Variation of average integrated RMS error on pupil phase and CTF with SNR. (Right) Convergence plots for Algorithms 1 and 2, showing the total RMS error between the true and retrieved IPSF versus the number of algorithm iterations.

to mention that in simulations performed, total RMS errors for Algorithm 2 remain at low levels of $< 10^{-3}$, whereas those achieved using Algorithm 1 are increased to $\sim 2 \times 10^{-3}$.

Figure 6 shows the results of Algorithm 2, when applied to a synthetic image set over a field of view of 10 μm × 10 μm × 20 μm. The larger axial field of view was used so as to improve the axial resolution of the retrieved CTF and to avoid effects associated with truncating the IPSF, however, sampling distances were held constant. Specifically, the upper panels of Figure 6 depict the amplitude of the simulated and retrieved CTF in the $n = 0$ plane (left) and through the $s = -1.8/\lambda$ plane (right), where the negative sign arises from the reflection geometry. Similarly, the lower panels show the corresponding phase of the CTF. Minor discrepancies can be seen between the true and retrieved CTF, however, these predominantly occur for spatial frequencies with low transmittance, such that the differences are not physically important. For simulations with Algorithm 2, no smoothing operations were performed and only a finite NA constraint was imposed. Finally, and in a similar vein to the Monte Carlo calculations performed for Algorithm 1, the noise tolerance of Algorithm 2 was also investigated by corrupting the input synthetic images with additive Gaussian noise of varying SNR. To quantify the performance of Algorithm 2, the mean integrated RMS error between the true and retrieved CTF averaged over 200 noise realizations was calculated and is again plotted in Figure 5.

Conclusions

In this paper, two algorithms, capable of retrieving either the complex pupil function, or the 3D CTF of a coherent reflection mode confocal imaging system from measurements of the IPSF, have been proposed and detailed. Algorithm 1, designed to achieve the former, essentially builds upon existing phase retrieval algorithms in incoherent imaging, such as fluorescence microscopy, however, the dependence of image formation in coherent confocal imaging on multiple pupils leads to the need to modify the update function in existing algorithms.

Algorithm 1, in principle, can operate with as few as two confocal image planes, however due to increased redundancy and noise suppression afforded by the averaging inherent in the algorithm, more image planes are preferable. Multiple image planes however present the opportunity to directly extract the full 3D imaging properties of the confocal set-up, as described by the CTF. This is the remit of Algorithm 2, which was shown to give comparable performance to Algorithm 1 in noise-free scenarios. Simulations suggest, however, that Algorithm 2 is more robust to noise present on input image data. That said, the performance in comparison to Algorithm 1, is in practice a balance between reduced noise amplification and reduced averaging and so careful consideration must be given to these points when setting image sampling rates.

Finally, it is important to comment briefly on the issue of uniqueness of the solution found by the presented algorithms. Uniqueness in phase retrieval problems is covered extensively in the literature under an array of scenarios (see, e.g. Klibanov *et al.*, 1995, for a brief survey), however here it is noted that the general problem of determining the phase of a function from the modulus of its Fourier transform does not admit a unique solution, however, the constraint of a finite pupil, that is to say a band-limited function, greatly restricts the solution set. Within this class of constrained phase retrieval problems, the solution can be shown to be unique up to so-called "zero-flipping" (Walther, 1963). In this regard, both algorithms presented make no special efforts to avoid this ambiguity, however, in all cases simulated they were found to converge to the true solution. Ultimately, it is thus envisaged that this work not only allows quantitative phase studies in confocal microscopy in both biological and engineering measurement contexts, but also permits full system characterization and calibration, without the need to introduce additional optics.

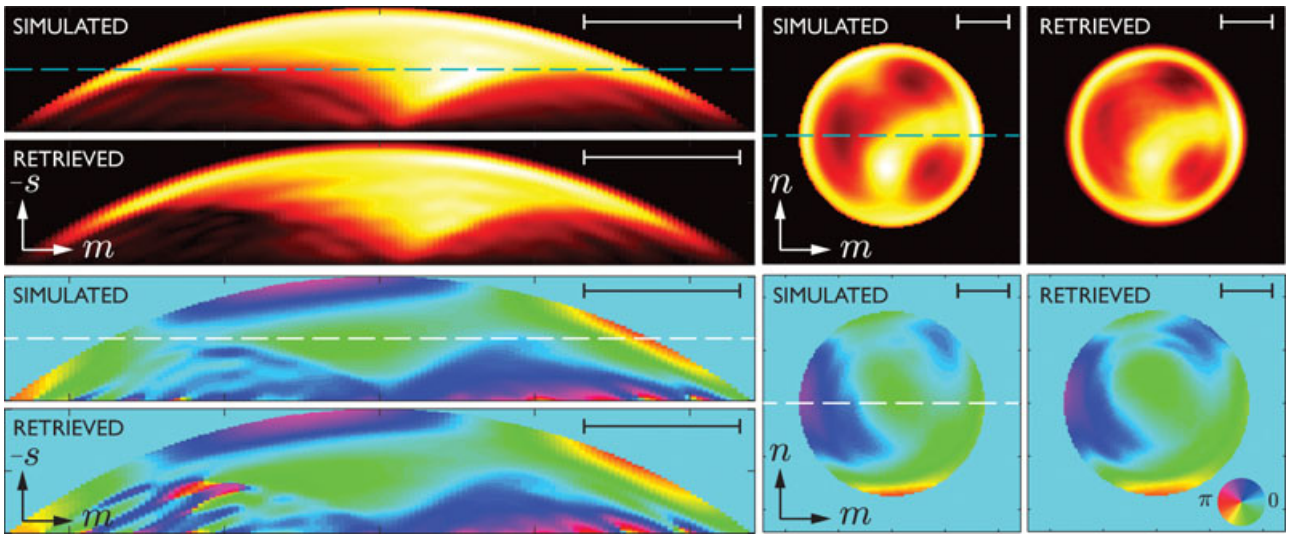

Fig. 6. Axial (left) and transverse (right) cross-sections, taken in the spatial frequency domain, of the amplitude (top panels) and argument (bottom panels) of the CTF determined by numerical evaluation of Eq. (7) and that retrieved from simulated intensity images of a point object using Algorithm 2. Dashed lines represent planes at which transverse and axial cross-sections were taken, respectively. Distance bars in all cases show a length of $1/(2\lambda)$.

Acknowledgements

Discussions with Drs. Kieran Larkin and Matthew Arnison, both with CISRA, Cannon, Australia and Prof. Tony Wilson at the University of Oxford, are gratefully acknowledged. M.R.F. acknowledges funding from an EPSRC KTS grant. C.L.G. and R.K.L. acknowledge funding from the BIS National Measurement System Engineering & Flow Metrology Programme 2011–2014.

References

Almoro, P., Pedrini, G. & Osten, W. (2006) Complete wavefront reconstruction using sequential intensity measurements of a volume speckle field. *Appl. Opt.* **45**, 8596–8605.

van der Avoort, C., Braat, J.J.M., Dirksen, P. & Janssen, A.J.E.M. (2005) Aberration retrieval from the intensity point-spread function in the focal region using the extended Nijboer-Zernike approach. *J. Modern Opt.* **52**, 1695–1728.

Beverage, J.L., Shack, R.V. & Descour, M.R. (2002) Measurement of the three-dimensional microscope point spread function using a Shack Hartmann wavefront sensor. *J. Micros.* **205**, 61–75.

Born, M. & Wolf, E. (1980) *Principles of Optics*. 7th edn. Cambridge University Press, Cambridge.

Cole, R.W., Jinadasa, T. & Brown, C.M. (2011) Measuring and interpreting point spread functions to determine confocal microscope resolution and ensure quality control. *Nat. Protoc.* **6**, 1929–1941.

Cotte, Y., Toy, M.F., Pavillon, N. & Depeursinge, C. (2010) Microscopy image resolution improvement by deconvolution of complex fields. *Opt. Expres.* **18**, 19462–19478.

Dändliker, R., Märki, I., Salt, M. & Nesci, A. (2004) Measuring optical phase singularities at subwavelength resolution. *J. Opt. A: Pure Appl. Opt.* **6**, S189–S196.

Foreman, M.R., Giusca, C.L., Coupland, J.M., Török, P. & Leach, R. (2013) Determination of the transfer function for optical surface topography measuring instruments: a review. *Meas. Sci. Technol.* **24**, 052001.

Gerchberg, R.W. & Saxton, W.O. (1972) A practical algorithm for the determination of the phase from image and diffraction plane pictures. *Optik* **35**, 237–250.

Giusca, C.L., Leach, R.K. & Helery, F. (2012) Calibration of the scales of areal surface topography measuring instruments: part 2: amplification, linearity and squareness. *Meas. Sci. Technol.* **23**, 065005.

Giusca, C.L., Leach, R.K., Helery, F., Gutauskas, T. & Nimishakavi, L. (2011) Calibration of the scales of areal surface topography measuring instruments: part 1: measurement noise and residual flatness. *Meas. Sci. Technol.* **23**, 035008.

Gu, M. (1996) *Principles of Three-Dimensional Imaging in Confocal Microscopes*. World Scientific, Singapore.

Gureyev, T.E., Roberts, A. & Nugent, K.A. (1995) Phase retrieval with the transport-of-intensity equation: matrix solution with use of Zernike polynomials. *J. Opt. Soc. Am.* **12**, 1932–1941.

Hanser, B.M., Gustafsson, M.G.L., Agard, D.A. & Sedat, J.W. (2003) Phase retrieval for high-numerical-aperture optical systems. *Opt. Lett.* **28**, 801–803.

Hanser, B.M., Gustafsson, M.G.L., Agard, D.A. & Sedat, J.W. (2004) Phase-retrieved pupil functions in wide-field fluorescence microscopy. *J. Microsc.* **216**, 32–48.

Juškaitis, R. & Wilson, T. (1997) The measurement of the amplitude point spread function of microscope objective lenses. *J. Microsc.* **189**, 8–11.

Klibanov, M.V., Sacks, P.E. & Tikhonravov, A.V. (1995) The phase retrieval problem. *Inv. Probl.* **11**, 1–28.

Leach, R.K., Giusca, C.L. & Coupland, J.M. (2012) Advances in calibration methods for micro- and nanoscale surfaces. *Proc. SPIE* **8430**, 84300H1–9.

Maiden, A.M. & Rodenburg, J.M. (2009) An improved ptychographical phase retrieval algorithm for diffractive imaging. *Ultramicroscopy* **109**, 1256–1262.

Mandal, R., Palodhi, K., Coupland, J.M., Leach R.K. & Mansfield, D. (2012) Application of linear systems theory to characterize coherence scanning interferometry. *Proc. SPIE* **8430**, 84300T1–10.

Marian, A., Charriére, F., Colomn, T., Montfort, F., Kühn, J., Marquet, P. & Depeursinge, C. (2006) On the complex three-dimensional amplitude point spread function of lenses and microscope objectives: theoretical aspects, simulations and measurements by digital holography. *J. Microsc.* **225**, 156–169.

Migukin, A., Katkovnik, V. & Astola, J. (2011) Wave field reconstruction from multiple plane intensity-only data: augmented Lagrangian algorithm. *J. Opt. Soc. Am.* **28**, 993–1002.

Pedrini, G., Osten, W. & Zhang, Y. (2005) Wave-front reconstruction from a sequence of interferograms recorded at different planes. *Opt. Lett.* **30**, 833–835.

Quirin, S., Pavani, S.R.P. & Piestun, R. (2012) Optimal 3D single-molecule localization for superresolution microscopy with aberrations and engineered point spread functions. *Proc. Natl. Acad. Sci. USA* **109**, 675–679.

Sakamoto, J.A. & Barrett, H.H. (2012) Maximum-likelihood estimation of parameterized wavefronts from multifocal data. *Opt. Expres.* **20**, 15928–15944.

Schrader, M. & Hell, S.W. (1996) Wavefronts in the focus of a light microscope. *J. Microsc.* **184**, 143–148.

Selligson, J.L. (1981) *Phase measurement in the focal region of an aberrated lens*. PhD thesis, University of Rochester, New York.

Stallinga, S. & Rieger, B. (2010) Accuracy of the Gaussian point spread function in 2D localization microscopy. *Opt. Expres.* **18**, 24461–24476.

Török, P. & Kao, F.-J. (2002) Point-spread function reconstruction in high aperture lenses focusing ultra-short laser pulses. *Opt. Commun.* **213**, 97–102.

Walford, J.N., Nugent, K.A., Roberts, A. & Scholten, R.E. (2002) High-resolution phase imaging of phase singularities in the focal region of a lens. *Opt. Lett.* **27**, 345–347.

Walther, A. (1963) The question of phase retrieval in optics. *Opt. Act.* **10**, 41–49.

Zhou, H. & Sheppard, C.J.R. (1997) Aberration measurement in confocal microscopy: phase retrieval from a single intensity measurement. *J. Modern Opt.* **44**, 1553–1561.